Melting efficiency of troilite-iron assemblages in shock-darkening : insight from numerical modeling

Moreau, Juulia-Gabrielle

2018-09

Moreau , J-G , Kohout , T & Wünnemann , K 2018 , ' Melting efficiency of troilite-iron assemblages in shock-darkening : insight from numerical modeling ' , Physics of the Earth and Planetary Interiors , vol. 282 , pp. 25-38 . https://doi.org/10.1016/j.pepi.2018.06.006

http://hdl.handle.net/10138/238342
https://doi.org/10.1016/j.pepi.2018.06.006

Physics of the Earth and Planetary Interiors 282 (2018) 25–38

Contents lists available at ScienceDirect

Physics of the Earth and Planetary Interiors

journal homepage: www.elsevier.com/locate/pepi

Melting efficiency of troilite-iron assemblages in shock-darkening: Insight from numerical modeling

Juulia-Gabrielle Moreau[a,*], Tomas Kohout[a,b], Kai Wünnemann[c]

[a] Department of Geosciences and Geography, University of Helsinki, P.O. Box 64, FI-00014 Helsinki, Finland
[b] Institute of Geology, The Czech Academy of Sciences, Rozvojová 269, CZ-165 00 Prague 6 – Lysolaje, Czech Republic
[c] Museum für Naturkunde, Leibniz Institute for Evolution and Biodiversity Science, Invalidenstraße 43, 10115 Berlin, Germany

ARTICLE INFO

Keywords:
Shock-darkening
Shock physics
Ordinary chondrites
Shock metamorphism
iSALE

ABSTRACT

We studied shock-darkening in ordinary chondrites by observing the propagation of shock waves and melting through mixtures of silicates, metals and iron sulfides. We used the shock physics code iSALE at the mesoscale to simulate shock compression of modeled ordinary chondrites (using olivine, iron and troilite). We introduced FeS-FeNi eutectic properties and partial melting in a series of chosen configurations of iron and troilite grains mixtures in a sample plate. We observed, at a nominal pressure of 45 GPa, partial melting of troilite in all models. Only few of the models showed partial melting of iron (a phase difficult to melt in shock heating) due to the eutectic properties of the mixtures. Iron melting only occurred in models presenting either strong shock wave concentration effects or effects of heating by pore crushing, for which we provided more details. Further effects are discussed such as the frictional heating between iron and troilite and the heat diffusion in scenarios with strongly heated troilite. We also characterized troilite melting in the 32–60 GPa nominal pressure range. We concluded that specific dispositions of iron and troilite grains in mixtures allow for melting of iron and explain why it is possible to find a wide textural variety of melted and unmelted metal and iron sulfide grains in shock-darkened ordinary chondrites. We finally observe shock-melting of albite within a few iron and troilite grain models, and investigate the effects of higher porosity within the olivine matrix in the single iron and troilite grain models.

1. Introduction

Shock-darkening in ordinary chondrites is the result of melting of iron sulfides and metals forming networks of tiny melt veins within silicates (Heymann, 1967; Britt et al., 1989; Britt and Pieters, 1989, 1994; Keil et al., 1992). These veins render the material darker and alter the reflectance spectra (Kohout et al., 2014). In shock-darkened meteorites, silicates can melt to form melt pockets and/or mix with the iron sulfides and metals, but the amount of silicate melt typically remains small.

In Moreau et al. (2017), we studied the effects of shock compression in ordinary chondrites using the iSALE shock physics code (Wünnemann et al., 2006) to assess the pressure range for shock-darkening. We used a so-called mesoscale approach that resolves sub-mm individual grains of metals and iron sulfides in ordinary chondrites. In that study we suggest that shock-darkening occurs between 40 GPa and 50 GPa with the exclusive melting of iron sulfides. However, several studies (Stöffler et al., 1991; Schmitt, 1995, 2000; Xie et al., 2014) claim that shock-darkening can involve melting of metals as well. Though it is known that metallic iron is difficult to melt by shock compression (Brown et al., 1984; Ahrens et al., 1998), several alternative mechanisms are possible to induce melting of metals and other phases within a shock physics mesoscale modeling approach using iron (kamacite), troilite, olivine and albite:

1. The eutectic temperature of FeNi + FeS is very low (Mare et al., 2014); these are mixed together in many ordinary chondrites (e.g. Tomkins, 2009).
2. Frictional heating (e.g. Stöffler et al., 1991; van der Bogert et al., 2003) is a mechanism that causes localized melting at material boundaries or between cracks. In mesoscale models, usually, only internal friction is considered. In this work we try to observe situations where frictional heating may occur along material interfaces.
3. Heat diffusivity is an important effect after shock. Because the iSALE mesoscale modeling does not consider heat diffusion after shock, in this work we only provide temperature contrasts between iron and troilite. We also touch on the heating of olivine or albite, because

* Corresponding author.
E-mail address: juulia.moreau@helsinki.fi (J.-G. Moreau).

https://doi.org/10.1016/j.pepi.2018.06.006
Received 25 October 2017; Received in revised form 7 May 2018; Accepted 25 June 2018
Available online 26 June 2018

they can either act as a heat source or sink for iron or troilite.
4. Metal grain shapes were studied in Moreau et al. (2017) and promising results were found with respect to the grain elongation in iron grains. In this study we investigate this effect on mixtures of metals and iron sulfides.
5. Pore crushing is a mechanism that generates very localized heating (Güldemeister et al., 2013). We will investigate this effect on iron in more details and see how it influences its melting.
6. Porosity affects the post-shock heating of a given phase. We investigate porosity in olivine (representing the silicate coarse-grained matrix) at 6% porosity (considering, e.g., ordinary chondrites of high petrographic types or intermediate shock stages, Consolmagno et al., 1998, Consolmagno et al., 2009). In addition we investigate 15% porosity in olivine (which corresponds to the upper range of measured or modeled porosities in ordinary chondrites; Consolmagno et al., 1998, Britt et al., 2002, Britt and Consolmagno, 2003, Sasso et al., 2009, Consolmagno et al., 2009). Such porosities are representative for ordinary chondrites that have been processed (shock compacted, or thermally metamorphosed) since the formation of the early Solar System. Such material likely experienced multiple shock events in the course of their evolution. However, precursors of ordinary chondrites show very high porosities (Bland et al., 2014 and references therein), which is why we also investigate the effect of 60% porosity in olivine on the temperatures contrast with iron or troilite inclusions.
7. Plagioclases are low density minerals, showing high impedance contrasts with the surrounding materials (here: olivine, iron, troilite). We investigate the effects of shock wave propagation between albite and the aforementioned materials, and the heating of albite as a source or sink for heating. Albite is often found conjointly melted with metals or iron sulfides (Figs. 1 and 2 in Tomkins et al., 2013 for metals)

By improving the iSALE mesoscale modeling code, we are able to investigate the effects of eutectic mixtures, grain shapes, and pore crushing more quantitatively. We improve thermal properties such as the heat capacities as a function of temperature in the determination of post-shock temperatures, which was considered as a constant in previous studies (Artemieva and Ivanov, 2005; Fritz et al., 2005; used in e.g. Meyer et al., 2011; Moreau et al., 2017). We also make a simple approach to consider the heat of fusion upon melting. With this improvement we expect to estimate the melt fractions and post-shock temperatures of the materials more accurately. With the new procedure, we will focus in detail on grain configurations found in ordinary chondrites at small scales (generally below 100–200 μm), thus applying the model to mixtures of metals and iron sulfides, and adjoining open pores in some models. In addition, we provide more insights into effects of shock wave propagation, how a shock wave interacts with phase interfaces (impedance contrasts), and how it can be concentrated by the geometry of the grains to enhance pressures (localized heating).

2. Methods

We present a suite of models of shock compression in several grain configurations of heterogeneous materials mimicking ordinary chondrites composition at the micrometer scale (mesoscale). We study the partial melting of phases associated with the increase in entropy by the shock wave, the reflection and refraction of shock waves at mineral phase boundaries, and the effects of localized heating (hotspots) due to pore crushing (Güldemeister et al., 2013). We use the iSALE-2D shock physics code (Wünnemann et al., 2006), which is based on the SALE hydrocode solution algorithm (Amsden et al., 1980). To simulate hypervelocity impact processes in solid materials, SALE was modified to include an elastic-plastic constitutive model, fragmentation models, various equations of state (EoS), and multiple materials (Melosh et al., 1992; Ivanov et al., 1997). More recent improvements include a modified strength model (Collins et al., 2004) and a porosity compaction model (Wünnemann et al., 2006; Collins et al., 2011).

We use a planar 2-D Eulerian frame of reference (Collins et al., 2013) to conduct mesoscale simulations of shock wave propagation. Analogous to so-called shock recovery experiments (e.g. Langenhorst and Deutsch, 1994, Langenhorst and Hornemann, 2005), we generate the shock wave by impacting a flyer plate on top of a series of layers: the buffer plate, the sample plate, and a secondary buffer plate. This approach has been previously used to describe shock propagation in heterogeneous materials by e.g. Crawford et al. (2003), Ivanov (2005), Riedel et al. (2008), Borg and Chhabildas (2011), Güldemeister et al. (2013), Bland et al. (2014), Davison et al. (2016) and Moreau et al. (2017). The model setup is identical to the setup used in Davison et al. (2016) and Moreau et al. (2017) where details are provided on the method and numerical setup. The flyer plate and sub-layers are made of olivine with the heterogeneities such as inclusions of different mineral phases or open pores embedded in the olivine sample plate. The flyer plate impacts the sub-layer at a given velocity, which generates a constant pressure (nominal pressure) into olivine. Materials used in this study, which are the main components of ordinary chondrites, are:

1. olivine, using the Analytical Equations of State (ANEOS, Thompson, 1990; Melosh, 2007) available in the iSALE code. Olivine was used as the silicate matrix material, including pyroxenes (similar to olivine in shock properties, Moreau et al., 2017). In the olivine sample plate, inclusions composed of the following materials are embedded:
2. iron (ANEOS) as the FeNi alloy kamacite in grains and,
3. troilite, using Tillotson equations of state with parameters described in Moreau et al. (2017), as the iron sulfide, in grains.
4. albite, using Tillotson equations of state, as the plagioclase. We describe the generation of the Tillotson equations of state similar to that used in Moreau et al. (2017), and the setting of other properties for albite in the Supplementary Material (McQueen et al., 1967, Melosh, 1989, Trunin, 2001, Benusa et al., 2005). We use albite as inclusion in some specific models.

All material parameters are listed in Table A1 (see Supplementary Material). We use a cylindrically symmetric grid in the models where the configuration of heterogeneities allows for it. In models, where the geometry and configuration of heterogeneities is asymmetric, we utilize a planar grid. A cylindrical grid better approximates 3-D effects on the convergence of shock waves, e.g. when pores collapse and pressure peaks are generated (Güldemeister et al., 2013). More details are given in the Supplementary Material on the use of cylindrical symmetry and resulting issues.

To simplify the setup of complex configurations of arbitrary grain shapes and pores, the iSALE code offers the possibility to use predefined images of the distribution and geometry of inclusions and pores that can be generated manually by any image processing software. Bitmaps (BMP-files), where the RGB-value defines different materials, can be loaded into iSALE to setup the model.

The suite of 20 models we have carried out for this study contains different configurations of troilite and iron grains, listed in Table 1 with their respective geometry, resolution, information on the mixture, and modeling parameters. These configurations are comparable to real grain configurations of meteorites. In Fig. 1 we compile a series of snapshots from meteorite backscattered electron microscope images depicting metal and iron sulfide grains to which we associate the corresponding 20 models. Some of these snapshots depict grains that are a result of shock melting, but a meteorite can record several shock events and, thus, any configuration can be present during shock compression. In Table 1, in addition to the 20 models, we describe 6 other models (21–26) which include an albite layer, an albite grain, and 4 configurations of models no. 1 and no. 5 with a half grain of albite. We compile models 21–26 sample plates in Fig. 2.

Table 1
List of models and their configuration.

No.	Geometry	Resolution	Details	Eutectic	Modeling duration time (ns)[b]	Model dimension (cells)[c]
1	2D cylindrical	65 CPGR[a]	*Iron grain*		110	200 × 641
2	2D cylindrical	65 CPGR	*Troilite grain*		110	200 × 641
3	2D cylindrical	50 CPGR	*Iron grain on top of troilite grain (olivine interface between)*		110	200 × 641
4	2D cylindrical	50 CPGR	*Troilite grain on top of iron grain (olivine interface between)*		110	200 × 641
5	2D cylindrical	50 CPGR incl., 85 'CPGR' ext. grain	*Iron grain within troilite grain*	x	110	200 × 641
6	2D cylindrical	50 CPGR incl., 85 'CPGR' ext. grain	*Troilite grain within iron grain*	x	110	200 × 641
7	2D cylindrical	65 CPGR	*Grain with top-half as iron*	x	110	200 × 641
8	2D cylindrical	65 CPGR	*Grain with top-half as troilite*	x	110	200 × 641
9	2D planar	65 CPGR	*Grain with left-part as troilite*	x	110	200 × 641
10	2D planar	85 CPGR	*Grain divided in 4 quadrants alterning iron and troilite*	x	110	200 × 641
11	2D cylindrical	85 CPGR (33 × 78 incl.)	*Iron grain with 4 rounded troilite inclusions on grain border*	x	110	200 × 641
12	2D cylindrical	85 CPGR (33 × 78 incl.)	*Troilite grain with 4 rounded iron inclusions on grain border*	x	110	200 × 641
13	2D cylindrical	75 × 32 CPGR incl., 60 × 50 'CPGR' ext. grain	*Oblate iron inclusion within oblate troilite grain*	x	110	200 × 641
14	2D cylindrical	75 × 32 CPGR incl., 60 × 50 'CPGR' ext. grain	*Oblate troilite inclusion within oblate iron grain*	x	110	200 × 641
15	2D cylindrical	32 × 75 CPGR incl., 50 × 60 'CPGR' ext. grain	*Prolate iron inclusion within prolate troilite grain*	x	117	200 × 681
16	2D cylindrical	32 × 75 CPGR incl., 50 × 60 'CPGR' ext. grain	*Prolate troilite inclusion within prolate iron grain*	x	117	200 × 681
17	2D cylindrical	25 CPGR incl. in 120 × 240 cells grain	*Mosaic of 9 rounded iron grains in rectangular rounded troilite grain*	x	220	400 × 1281
18	2D cylindrical	25 CPGR incl. in 120 × 240 cells grain	*Mosaic of 9 rounded troilite grains in rectangular rounded iron grain*	x	220	400 × 1281
19	2D cylindrical	30 × 60 cells square pore	*Empty pore atop an iron layer*		220	400 × 1281
20	2D cylindrical	30 × 60 cells square pore	*Empty pore beneath an iron layer*		220	400 × 1281
21	2D cylindrical	–	*Olivine sample plate replaced by albite*		110	200 × 641
22	2D cylindrical	65 CPGR	*Albite grain*		110	200 × 641
23	2D cylindrical	65 CPGR, 95 'CPGR' half-grain	*Iron grain with half-grain of albite above*		110	200 × 671
24	2D cylindrical	65 CPGR, 95 'CPGR' half-grain	*Iron grain with half-grain of albite below*		110	200 × 671
25	2D cylindrical	50 CPGR incl. in 85 'CPGR' grain, 116 'CPGR' ext. half-grain	*Iron grain within troilite grain with half-grain of albite above*	x	110	200 × 671
26	2D cylindrical	50 CPGR incl. in 85 'CPGR' grain, 116 'CPGR' ext. half-grain	*Iron grain within troilite grain with half-grain of albite below*	x	110	200 × 671

[a] CPGR: Cells per grain radius. 'CPGR', relative to center of the configuration.
[b] iSALE modeling time-step: 0.15 ns.
[c] Cell size: 1 μm.

2.1. Peak shock pressure recording

Peak shock pressures are recorded within Lagrangian tracers. The displacement of tracers is calculated by the material flux through the cell faces (Davison et al., 2016). To assess post-shock temperatures, we use the maximum pressure each tracer experiences during the passage of the shock wave. Care has to be taken as the shock-induced increase in entropy is lower if it is caused by a multiple shock wave (ramping up the shock pressures as in reverberating shock experiments, Langenhorst and Hornemann, 2005; Prescher et al., 2011) rather than by a single shock wave, if both shocks attain the same final pressure. Because reflections happen at boundaries between materials of different densities (impedance contrasts), we determine the average between the pressure of the first shock wave and the superimposing subsequent pressure pulses, in the tracers, to approximately account for reverberation effects. The biggest increase in entropy usually results from the first shock wave and subsequent reflections give only a minor contribution to the increase in entropy. In early tests we found a decrease of, e.g., ~60 K and ~ 4 GPa in troilite using the peak shock pressures average out from a reflection from iron to troilite in model no. 8. Although this is a rather crude approach, we use this method to estimate the post-shock temperature in the present study and we consider our approach to be sufficiently accurate. However, we account for localized shock pressure amplification due to the closure of pores (models 19–20) as described in Güldemeister et al. (2013) by considering only the last recorded peak shock pressure from reflections.

2.2. Thermal properties and post-shock temperatures

As stated above we use the peak shock pressures recorded in tracers to estimate post-shock temperatures. We do not rely on post-shock temperatures given by the EoS in iSALE for several reasons: first, we had to use different EoS (Tillotson and ANEOS as described above), and temperature estimates from Tillotson EoS tends to be inaccurate. Second, we take into account that thermodynamic properties such as the heat capacity are a function of temperature, whereas in the Tillotson EoS, heat capacity is considered as a constant. Third, we consider the heat of fusion at melting, which is not accounted for in both Tillotson EoS and ANEOS.

To assess post-shock temperatures, the peak shock pressures are first converted to a total energy E_{total} (J kg^{-1}, the specific energy) at the shock stage and after the subsequent release; the procedure is described in Moreau et al. (2017) and references therein. This technique provides a good approximation of the total specific energy E_{totab} except the discussed inaccuracies in Moreau et al. (2017).

For each material we integrate the heat capacities as a function of temperatures (iron, Desai, 1986; troilite, Chase, 1998; olivine, Gillet, 1991; albite, Hemingway et al., 1981) up to the melting point to assess

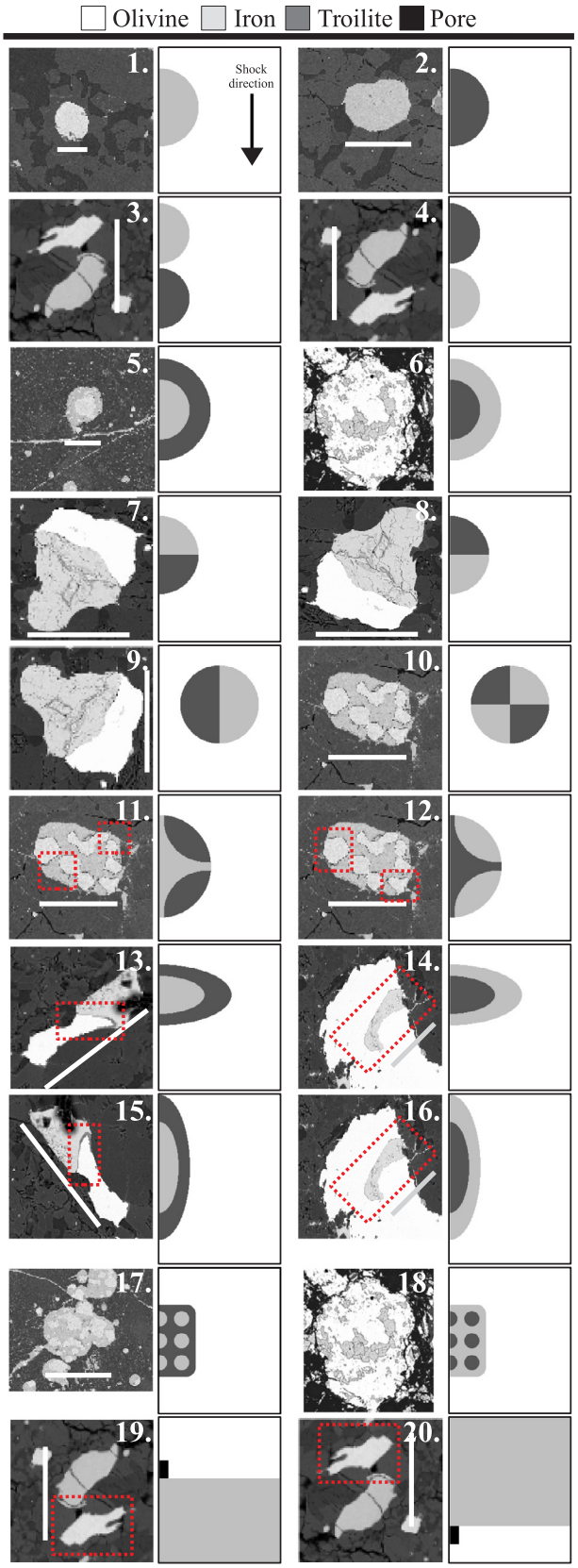

Fig. 1. Compilation of all 20 models without albite. Each duo of figures represents: a) a snapshot from a backscattered electron microscope thin section, b) the initial sample plate used in the models and material within (BMP file) determined by the upper-left color codes. All models numbers are the same as in Table 1. The red dashed-boxes in the snapshots emphasize the areas of interest that can compare with the models. In the backscattered electron microscope snapshots metals are brighter than iron sulfides within the darker silicate matrix and empty pores (black). Scales (white lines) and origins of the chondrite snapshots are: Annama H5 (3, 4, 19, 20, at 118 µm), Chantonnay L6 (1, at 40 µm; 2, at 76 µm; 5, at 43 µm; 10–12, at 102 µm), and Supuhee H6 (7–9, at 125 µm; 13, 15, at 148 µm; 14, 16, at 57 µm) ordinary chondrites. Models no. 6 and no. 18 snapshots originate from an enstatite chondrite (Sahara 97072, EH3, Lehner et al. 2010, modified, scale unknown). Though some of these configurations are products of shock or thermal effects, meteorites can record several shock events and such grains can be found in any meteorite prior to such events. The shock wave propagation direction is indicated by the black arrow in the first model sample plate.

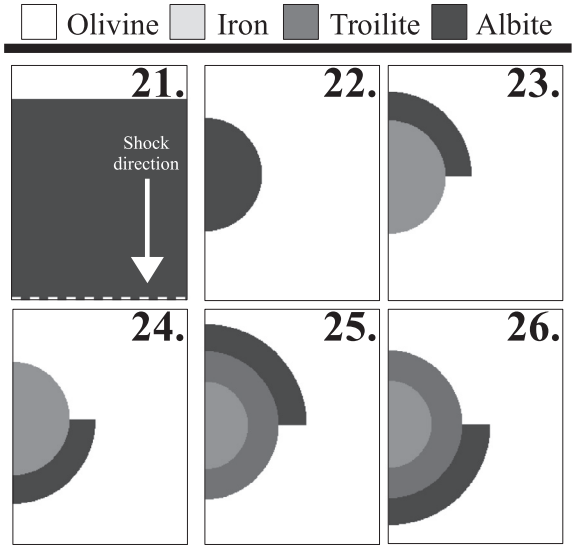

Fig. 2. Compilation of models 21–26 sample plates with albite. The shock wave propagation direction is indicated by the black arrow in the first model sample plate. The dashed white line in model no. 21 indicates that the albite layer is continuous to the bottom buffer plate. The top buffer plate remains unchanged (olivine) in the models.

post-shock temperatures with better accuracy. We also include the heat of fusion at the melting point (iron, metallurgical value; troilite, Sharp, 1969; olivine, Kojitani and Akaogi, 1995, albite, Tenner et al., 2007) to estimate the amount of partial melting of each material and to avoid over-estimation of temperature at the melting point. Using the energies involved in shock compression we determined three phases to calculate the post-shock temperature ($T_{post\text{-}shock}$) and melt fraction (α):

$$T_1 \approx \frac{E_{total}}{\overline{c}_p} \quad \text{with } E_{total} \approx \sum_{T_0}^{T_1} c_p \Delta T \text{ and } T_1 \leqslant T_{melt}, \tag{1}$$

which is the first phase of temperature increase until the melting point T_{melt} where c_p are the heat capacities (J kg^{-1} K^{-1}) of the material at temperature T. To obtain the post-shock temperature T_1, the specific energy E_{total} is divided by the average of all heat capacities; the averaged heat capacities are determined for each ΔT interval, starting from T_0 (equal to 293 K, Moreau et al., 2017), until their sum approaches the E_{total} value (right hand-side of Eq. (1)). T_1 corresponds to the temperature increase up to the onset of melting.

$$\alpha = \frac{E_{total} - \sum_{T_0}^{T_{melt}} c_p \Delta T}{H_f} \quad \text{with } 0 \leqslant E_{total} - \sum_{T_0}^{T_{melt}} c_p \Delta T \leqslant H_f, \tag{2}$$

which is the second phase of partial melting. The excess of integrated specific energy over the melting point, once the melting point is reached in Eq. (1), is divided by the heat of fusion ($J\,kg^{-1}$), H_f, to obtain the fraction of melt α. There is no rise of temperature during this phase as the remaining specific energy is consumed by melting of matter.

$$T_2 = \frac{E_{total} - H_f - \sum_{T_0}^{T_{melt}} c_p \Delta T}{c_{p\ at\ T_{melt}}} \quad \text{with } E_{total} - \sum_{T_0}^{T_{melt}} c_p \Delta\ T > H_f, \tag{3}$$

is the third phase if complete melting is achieved (α = 1). The increase of temperature T_2 is simply given by the remaining specific energy from Eqs. (1) and (2) divided by a constant heat capacity above the melting point (no varying heat capacity of liquid material is considered). The material does not necessarily reach the second or third phase.

$$T_{post-shock} = T_0 + T_1 + T_2, \tag{4}$$

is the total post-shock temperature of the material from Eqs. (1) and (3) to which is added the initial temperature of the model, T_0. The multiplications by ΔT in Eqs. (1)–(3) represent the 1 K interval for summing heat capacities and to convert heat capacities to an equivalent specific energy.

To analyze eutectic mixtures, we applied heat of fusion ($285\,kJ\,kg^{-1}$, H, L and LL ordinary chondrites average, Mare et al., 2014) and melting temperature (1261 K, Sharma and Chang, 1979; Tomkins, 2009; Mare et al., 2014) for iron and troilite. For both iron and troilite, in Eq. (1), T_{melt} is replaced by the eutectic melting temperature and, in Eq. (2), H_f is replaced by the eutectic heat of fusion. We varied heat capacities over temperature for iron and troilite equal to the non eutectic materials, but only up to the eutectic melting temperature. The reason we treat troilite and iron separately, regarding their heat capacities, is because their different impedances affect the shock wave propagation and respective shock-induced increases in entropy. This is why we do not express the partial melting in the results as a percentage of the whole mixture, but for individual phases only. This is certainly a very simplified approach to account for the eutectic thermal properties of material mixtures, but it provides first-order estimates to assess the importance of this process.

2.3. Strength of materials

Our study relies on peak shock pressures to determine post-shock temperatures and we neglect temperature increase due to plastic work resulting from the closure of pores in the mesoscale models, where individual pores are resolved. However, we do use a strength model to account for a more realistic description of the response of materials to shock wave compression and the resistance of pores to be crushed. We briefly discuss the minor effect of strength on peak shock pressures in the Supplementary Material.

2.3.1. Troilite and albite

We use the von Mieses criterion for troilite (using pyrrhotite Hugoniot elastic limit of 3.5 GPa and Poisson's ratio of ~0.25, Louzada et al., 2010) and albite (using Hugoniot elastic limit of 4.5 GPa and Poisson's ratio of ~0.283, Ahrens and Gregson, 1964, Christensen, 1996). We estimated the yield strength σ_{yield} to be 2.3 GPa for troilite and 2.72 GPa for albite from Eq. (5) for longitudinal stress σ_L (Melosh, 1989):

$$\sigma_L = -\sigma_{HEL} = \frac{-(1-\nu)}{(1-2\nu)} \cdot \sigma_{yield} \tag{5}$$

where σ_{HEL} is the Hugoniot elastic limit, ν the Poisson's ratio. These rather high values for troilite or albite describe well the behavior of single crystals and as troilite grains are of small sizes, we consider it to be a good approximation.

2.3.2. Iron

We use literature Johnson-Cook strength model parameters for iron (Rajendran et al., 1990) with constants *A*: 175.12 MPa, *B*: 3799.9 MPa, *C*: 0.06, *n*: 0.32 and *m*: 0.55.

2.3.3. Olivine

We use strength properties (Table A1) from the literature (Brace, 1980; Bland et al., 2014; Perras and Diederichs, 2014; Christensen, 1996), which are described in detail in Collins et al. (2004). To represent a coarse-grained olivine matrix (e.g. 6% and 15% porous olivine), we arbitrarily assume a bulk cohesion of 111 MPa (peridotites, Perras and Diederichs, 2014). This is ten times smaller than in Bland et al. (2014), who chose a value of 1 GPa for chondrules. Other parameters are similar to Bland et al. (2014). The maximum strength (for infinite confining pressure) has been estimated by Brace (1980) for olivine under tensile or compressive stress. We kept it fixed at 1.5 GPa. For a 60% porous olivine, the bulk cohesion was modified to 100 kPa, accordingly to Bland et al. (2014).

2.4. Resolution

The iron and troilite grain resolution (cells per grain radius, CPGR) has to be chosen carefully to make sure that the obtained results are not affected by resolution (Davison et al., 2016). We increase the resolution proposed in Moreau et al. (2017), who showed that resolution in their work was sufficient (24 cells per grain radius, CPGR), to account for more localized effects of the pressure. The resolution for the rectangular pores edges is 60 cells. This value has been suggested by Güldemeister et al. (2013) to simulate localized heating due to the collapse of pores accurately.

3. Results

3.1. Models 1-20

We compile all results from the 20 models listed in Table 1, and illustrated in Fig. 1, into Table 2. We estimated the post-shock temperatures and melting as described above. For configurations approaching eutectic mixtures (models 5–18), we analyzed our model results using the simplified eutectic thermal properties. In addition to Fig. 1, where all 20 models are illustrated as sample plates, we also show the resulting post-shock temperatures and melt fractions α in a compressed state in Fig. 3, before the release wave has unloaded the sample to normal pressure. In Table 2 the following parameters are compiled for iron, troilite and olivine: peak shock pressures, post-shock temperatures, and information on the melting with the melt fraction α and the fraction of material that reaches melting temperature. The nominal pressure (the pressure recorded in the olivine buffer plate) for the suite of models is 45.2 GPa and lies in the pressure range proposed for shock-darkening (40–50 GPa, Moreau et al., 2017). The models no. 1 and no. 2 serve as reference cases with a spherical iron or troilite inclusion, respectively, with information on the pressure/temperature impedance with olivine in Fig. 3. The melt fraction values are mass weighted averages of all tracers particles for a given phase.

The results are as follows:

1. In all models troilite melts with a melt fraction α from 0.14 to 0.97. In model no. 2 the material starts to melt without any influence of iron or other specific configurations and melt fraction reaches value of 0.14. The melting is localized at the lower part of the grain. This is the case for all models where the concentration of melt is localized in that region, unless heterogeneities exist (models nos. 3, 5, 13, 15). The largest amount of melt is generated in eutectic models in which troilite is mostly embedded in iron (models nos. 6, 12, 14, 16, 18, with melt fraction α of 0.75, 0.83, 0.97, 0.75 and 0.94 respectively). In all models, troilite shows large fractions of completely molten

Table 2
Models 1–20 results.

Model	Iron							Troilite							Olivine						
	Peak shock pressure (GPa)[a]	*sd.*	*Post-shock temp. (K)*	*sd.*	*Melt frac. α*	*sd.*	*Fraction of material ≥ T_{melt} (%)*	*Peak shock pressure (GPa)*[a]	*sd.*	*Post-shock temp. (K)*	*sd.*	*Melt frac. α*	*sd.*	*Fraction of material ≥ T_{melt} (%)*	*Peak shock pressure (GPa)*[a]	*sd.*	*Post-shock temp. (K)*	*sd.*	*Melt frac. α*	*sd.*	*Fraction of material ≥ T_{melt} (%)*
1	66.49	4.95	827	60	0	0	0	–	–	–	–	–	–	–	47.78	5.58	879	129	0	0	0.00
2	–	–	–	–	–	–	–	59.81	9.46	1332	182	0.1412	0.3005	27.12	48.36	9.90	892	216	0.0081	0.0817	1.31
3	65.89	4.67	820	56	0	0	0.00	67.67	13.58	1446	280	0.4301	0.4203	60.88	47.02	7.20	862	152	0.0047	0.0650	0.60
4	88.25	22.37	1088	292	0.0351	0.1723	4.91	60.50	11.26	1358	271	0.1370	0.2956	26.71	47.50	7.71	873	174	0.0036	0.0569	0.49
5	67.12	2.25	835	27	0	0	0.00	63.59	9.61	1330	262	0.5250	0.3483	87.88	49.11	12.96	907	280	0.0158	0.1183	2.07
6	67.50	12.95	834	146	0.0062	0.0493	2.54	73.02	16.01	1582	540	0.7511	0.2918	99.95	49.05	7.47	906	170	0.0022	0.0314	0.65
7	63.43	2.96	790	36	0	0	0.00	58.96	13.30	1278	346	0.2995	0.4164	43.40	49.33	10.40	912	228	0.0084	0.0858	1.20
8	79.79	8.94	973	98	0	0	0.00	66.38	8.10	1374	167	0.6427	0.3341	98.71	47.55	5.53	874	128	0	0	0.00
9	60.61	2.70	756	33	0	0	0.00	56.46	4.01	1234	50	0.1621	0.2460	55.68	49.29	5.34	909	113	0	0	0.00
10	64.43	5.90	802	71	0	0	0.00	62.19	7.30	1273	117	0.5426	0.3501	85.64	49.97	5.63	923	119	0	0	0.00
11	72.42	8.07	895	89	0.0046	0.0598	0.77	64.21	7.86	1321	152	0.5928	0.3693	88.77	48.87	11.11	902	241	0.0104	0.0974	1.31
12	67.82	9.35	839	106	0	0	0.00	70.62	9.65	1449	281	0.8301	0.2797	97.31	48.60	6.22	896	142	0.0008	0.0191	0.28
13	65.57	2.31	816	28	0	0	0.00	56.64	6.37	1200	89	0.4943	0.3410	54.93	48.44	4.65	891	98	0	0	0.00
14	64.79	5.31	806	64	0	0	0.00	76.05	7.38	1584	245	0.9655	0.1003	100.0	49.74	5.19	918	110	0	0	0.00
15	82.23	5.49	1002	56	0.0006	0.0114	0.34	69.44	19.65	1539	676	0.5755	0.4211	80.53	47.19	8.71	866	198	0.0055	0.0699	0.76
16	73.54	27.96	882	290	0.1471	0.3385	17.66	74.17	21.28	1639	828	0.7502	0.3249	98.61	47.09	6.69	863	143	0.0039	0.0568	0.61
17	70.16	5.97	869	69	0	0	0.00	63.33	6.90	1296	119	0.5788	0.3557	88.23	48.09	8.01	887	180	0.0037	0.0520	0.75
18	69.06	11.00	854	126	0.0013	0.0244	0.46	73.34	9.11	1500	320	0.9424	0.1228	100.0	48.24	6.9	889	158	0.0008	0.0154	0.38
19	68.79	10.42	856	159	0.0051	0.0673	0.70	–	–	–	–	–	–	–	68.44	10.64	1331	259	0.0127	0.1054	1.81
20	65.88	2.84	820	40	0.0003	0.0169	0.04	–	–	–	–	–	–	–	44.72	14.47	823	311	0.0155	0.1187	1.94

[a] Nominal pressure (in olivine at buffer) is 45.2 GPa.

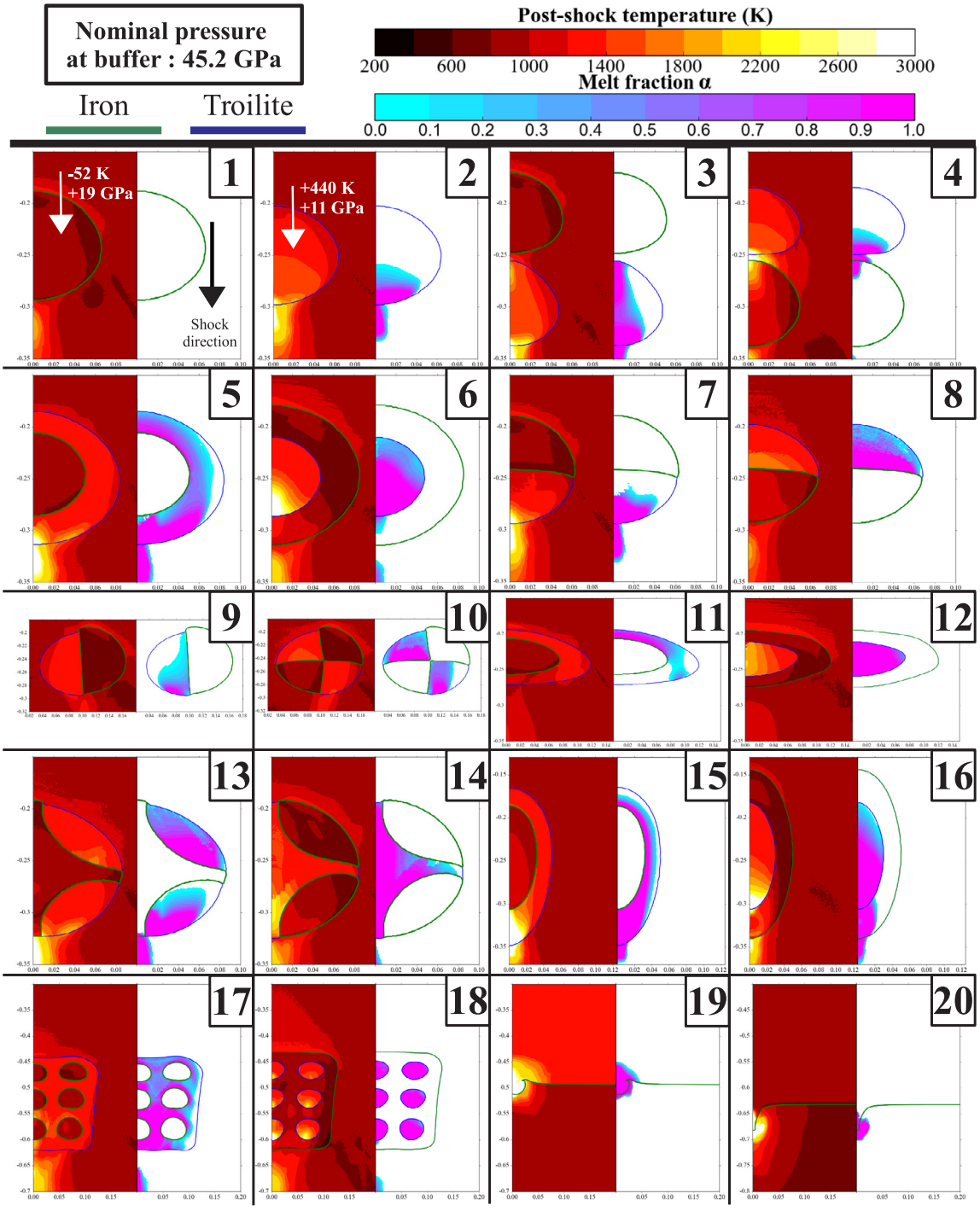

Fig. 3. Compilation of models 1–20. Each duo of figures represents: a) the post-shock temperature map, b) the melt fraction α map of the model. All figures are in a compressed state. All models have been run at 45.2 GPa of nominal pressure. All models numbers are the same as in Table 1 and Fig. 1. Models no. 19 and no. 20 are zoomed to the zones of interest. The shock wave propagation direction is indicated by the black arrow in the first model sample plate and contours of iron and troilite are indicated. Contrasts in peak shock pressure and post-shock temperature are indicated for models. no. 1 and no. 2. Graduations are in millimeters.

material with post-shock temperatures above the melting point (bright pink zones in melt fraction plots, Fig. 3). The highest recorded post-shock temperature is 1639 K (sd. = 828 K) in model no. 16.

2. Partial melting of iron occurs in eutectic models presenting convergence and superposition of shock waves from troilite grains (e.g. models nos. 6, 11, 16, 18) due to the complex geometry of the grains (see Discussion and Figs. 1 and 3). The typical melt fraction values are within the 0.00–0.15 interval. The highest melt fraction α, 0.15 (sd. = 0.34), is recorded in model no. 16, in which a prolate iron grain contains a prolate inclusion of troilite. Only one non-eutectic model (model no. 4) shows melting (α: 0.04 ± 0.17) in iron, due to the nearby troilite grain. Melting also occurs in the vicinity of the collapsed pore in model no. 19 within a really small area (0.70% of the whole layer only is melting, that makes about 780 tracers in the vicinity of the pore). Iron does not melt in the single iron grain model (model no. 1) and post-shock temperatures remain low in all models. The highest recorded post-shock temperature is 1088 K

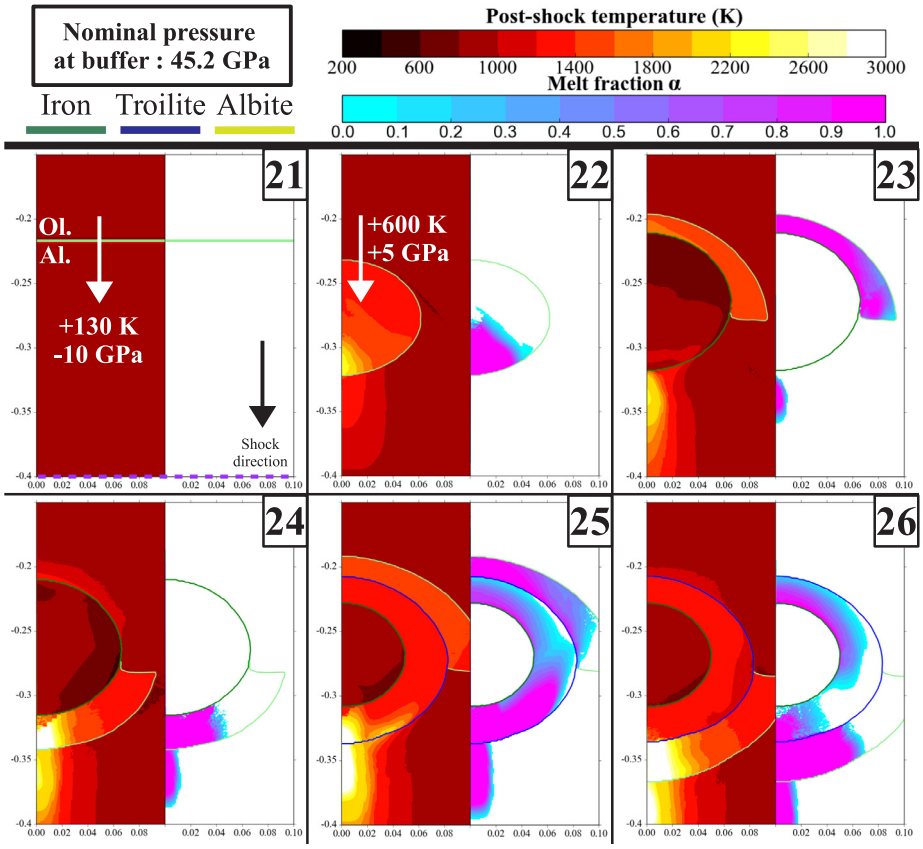

Fig. 4. Compilation of albite models 21–26. Each duo of figures represents: a) the post-shock temperature map, b) the melt fraction α map of the model. All figures are in a compressed state. All models have been run at 45.2 GPa of nominal pressure. All models numbers are the same as in Table 1 and Fig. 2. The shock wave propagation direction is indicated by the black arrow in the first model sample plate and contours of iron, troilite and albite are indicated. The purple line in bottom of model 21 indicates that the albite layer is continuous to the bottom buffer plate. Contrasts in peak shock pressure and post-shock temperature are indicated for models. no. 21 and no. 22. Graduations are in millimeters.

(sd. = 292 K) in model no. 4. All models with melting of iron show very localized melting.

3. Small fractions of olivine melt at conditions similar to iron in models nos. 2–7, 11–12, 15–20 with melt fraction α between 0.00 and 0.02. The recorded post-shock temperatures in olivine span from 862 K to 923 K and specifically 1331 K in model no. 19, but where olivine only makes up 41% of the sample plate (e.g. 70–80% in most models, 25% in model 20).

3.2. Models 21-26, albite

The results from the 6 additional albite models are compiled in Table A3, in the Supplementary Material. As for models 1–20, in addition to Fig. 2 where models 21–26 are illustrated, we show the resulting post-shock temperatures and melt fraction α in a compressed state in Fig. 4. The nominal pressure is equivalent to 45.2 GPa and models 21–22 act as references with a layer of albite (down the buffer plate) and a spherical grain of albite in olivine, with information on the pressure/temperature impedance with olivine in Fig. 4.

1. In models no. 25 and no. 26, troilite shows melt fraction α of 0.36 and 0.32, which shows a difference of −0.16 and −0.20 compared to the original model no. 5 that has the same iron and troilite configuration. However, peak shock pressures or post-shock temperatures are higher (+3 GPa, +59 K) in model no. 25 and lower (−5 GPa, −91 K) in model no. 26, compared to model no. 5.
2. In models no. 23 and no. 24, peak shock pressures or post-shock temperatures in iron are, as an example, higher (+0.5 GPa, +4 K) in model no. 23 and lower (−3 GPa, −37 K) in model no. 24, compared to model no. 1.
3. Melting of albite is observed in models 22–26 with melt fraction α varying from 0.25 to 0.84. Recorded peak shock pressures and post-shock temperatures vary from 51 GPa to 58 GPa and 1423 K to 1728 K. In model no. 21, which displays a planar shock in albite layer from an olivine buffer plate, pressure ratio between olivine (nominal pressure, 45.2 GPa) and albite is 1.23, which indicates the impedance contrast between the two materials; the post-shock temperatures are 954 K in albite and 824 K in olivine, in model no. 21.

4. Discussion

Shock wave interactions in iron and troilite mixtures appear to be important for melting of metals and their role in the shock-darkening process. In fact, in several models (e.g. models no. 4 and no. 16), we observe the convergence and superposition of shock waves that increase the peak shock pressures in the materials. In these models we observe an increased melting of iron. In our previous study (Moreau et al., 2017) we did not find melting of iron at 45 GPa of nominal pressure because no eutectic thermal properties were considered and all iron grains were isolated and rounded (such as in the present study model no. 1). The heating of individual phases (e.g. olivine, albite) may also influence surrounding material heating, such as iron. The models satisfactorily predict that iron melting can occur at this rather low pressure, in agreement with the observations of small amounts of molten metals present in shock-darkened meteorites (Stöffler et al., 1991). However, proportion of iron that melts remains low compared to troilite with up to a fifth of the melt fraction observed in troilite.

4.1. Pressure effects

To understand shock-induced heating of materials, one has to identify how pressure is amplified in areas where we observe stronger heating. In model no. 16, with a prolate troilite inclusion in iron, the peak shock pressures reach values of 74 GPa (sd. = 21 GPa) in troilite and 74 GPa (sd. = 28 GPa) in iron. The mechanism to achieve these

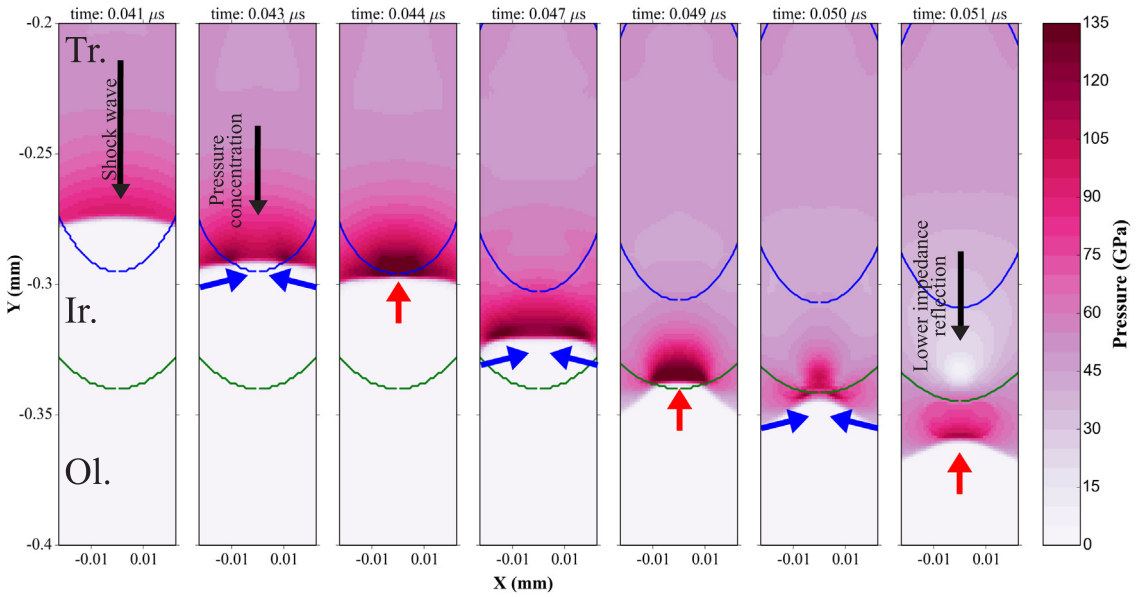

Fig. 5. Snapshots (model no. 16) of a shock wave traveling in the olivine (Ol.) sample plate through a prolate troilite (Tr.) inclusion within an iron (Ir.) prolate grain. The figure is centered to the lower part of the model. It shows concentration of the shock wave due to the cylindrical geometry and collisions due to shock wave velocity contrast (blue arrows) between convergent shock waves, leading to a strong rise in pressure (and temperature) locally (red arrows). The snapshots are manually mirrored from the original model at x: 0.00 to have a better view of the effects.

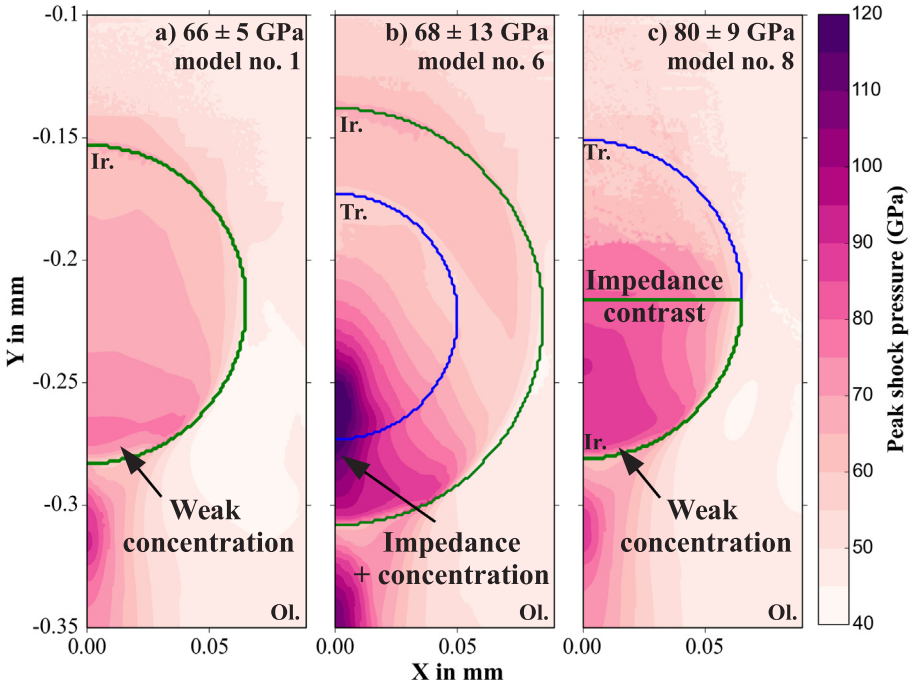

Fig. 6. Peak shock pressures in a) model no. 1 for iron, b) model no. 6 for an inclusion of troilite in iron, and c) model no. 8 for troilite atop of iron, illustrating the effect of impedance contrast from troilite to iron in rising the peak shock pressure (values are given in the panels for iron). It also illustrates the effect of pressure concentration as seen in Fig. 5. Iron is delineated in green and troilite in blue. The peak-shock pressures are displayed in the material before compression.

strongly localized pressures is illustrated in Fig. 5. It shows how the shock wave, which propagates faster in iron, travels around both sides of the troilite grain, converges and superimposes at the center on the opposite side of the inclusion, which causes the strong rise in pressure (see also Davison, 2008). This behavior is similar to convergent shock waves seen in spherical shock wave implosions (Kozlov and Petrovtsev, 2014). This focusing effect is attributed to the impedance contrast between troilite and iron (Hirose and Lonngren, 1985). If we compare the peak shock pressures in iron from models no. 1 (isolated), no. 6 (troilite inclusion) and no. 8 (iron beneath troilite), illustrated in Fig. 6, we observe that the effect of impedance contrast between troilite and iron in model no. 8 increases the peak shock pressures by 14 GPa in iron compared to model no. 1. However, there is a weaker amplification of pressures in model no. 8 compared to model no. 6 as the contact between iron and troilite in model no. 8 is planar and no superposition of shock waves happens nearby the boundary. The impedance contrasts and converging shock waves also explain the strong rise in iron peak shock pressures in model no. 4. In this model we observe the highest peak shock pressures in iron (88 GPa, sd. = 22 GPa) from all the suite of models. In Fig. 7 the shock wave propagation through model no. 4 is illustrated. This is similar to the shock wave propagation in model no. 16 (Fig. 5), but with an olivine interface between the troilite and iron grains that are, thus, not in contact. More details on the elongation ratio in prolate and oblate scenarios in iron are given in Moreau et al. (2017).

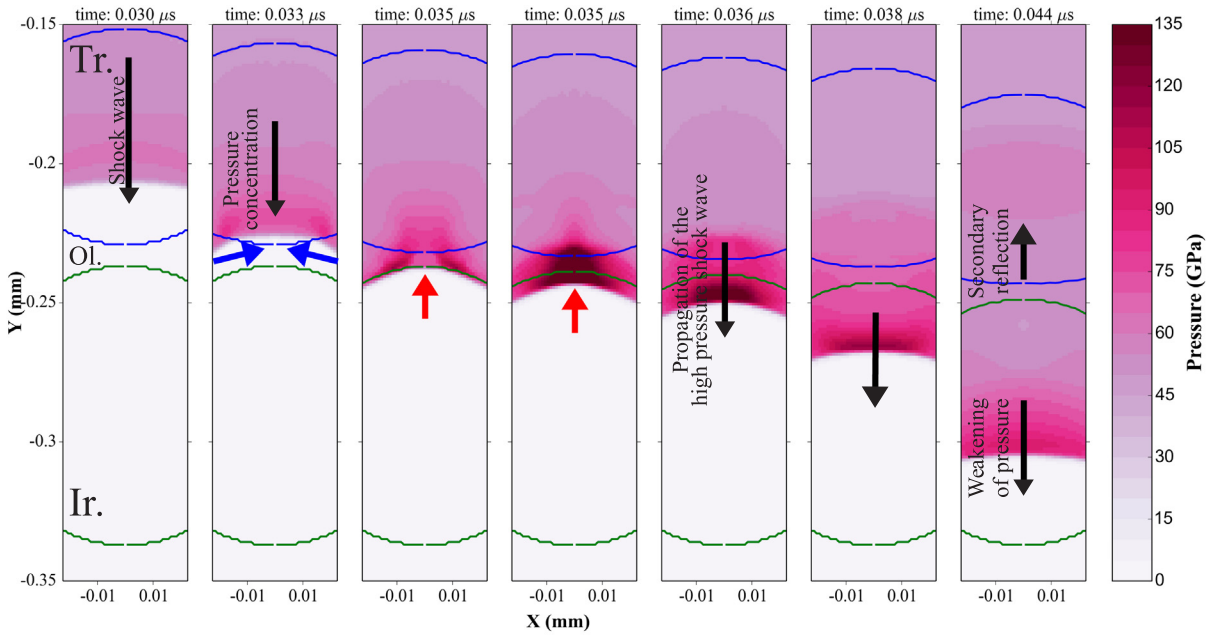

Fig. 7. Snapshots (model no. 4) of a shock wave traveling in the olivine (Ol.) sample plate through a troilite grain (Tr.) above an iron grain (Ir.) with an olivine interface between. The figure is centered to the model. It shows concentration of the shock wave due to the cylindrical geometry and collisions due to shock wave velocity contrast (blue arrows) between convergent shock waves, leading to a strong rise in pressure (and temperature) locally (red arrows). The snapshots are manually mirrored from the original model at x: 0.00 to have a better view of the effects.

The effects of pressure reflections (e.g. from iron, see also Moreau et al., 2017) or pressure concentrations, explained above (e.g. at the bottom of iron or troilite grains), both contribute to the heating of olivine. Hence, in most models (Figs. 3 and 7, especially model no. 4), olivine acts as a source for heating of iron either from the top (reflected pressures) or bottom (concentration of shock waves). In troilite, the olivine heat source mostly occurs at the bottom of the grains (Fig. 3) because troilite is usually hotter than olivine at the top boundary (e.g. model no. 2 in Fig. 3).

4.2. Frictional heating

In model no. 9, where troilite is adjacent to iron (planar contact), one can speculate on the effect of frictional heating. A contrast of ~300 m/s in particle velocity exists at the boundary between troilite and iron (see Fig. 8). This is expected to cause frictional heating and, eventually, melting of both components at the boundary (unless frictional heating is negligible due to low confining pressure or until melting occurs, which may have a lubrication effect reducing the coefficient of friction significantly, Melosh, 2005, Chen and Rempel, 2014). Frictional heating and melting could occur in all scenarios associated with high impedance contrasts, longitudinal or tilted to the planar shock front, and with large differences in particle velocity. Frictional heating is shown to produce localized shock-darkening in ordinary chondrites (Stöffler et al., 1991; van der Bogert et al., 2003).

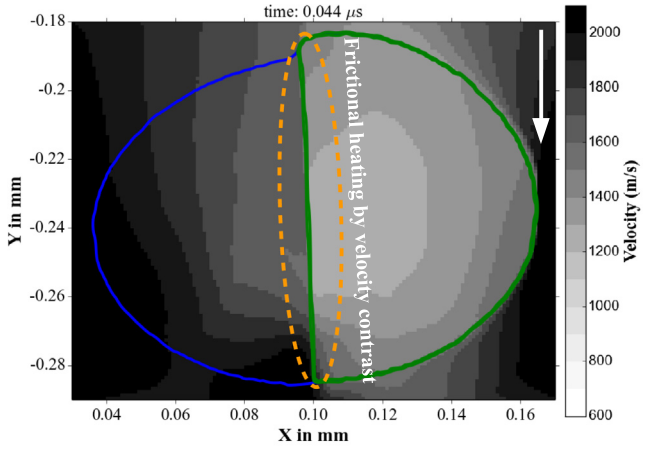

Fig. 8. Y-axis particle velocities of a grain of troilite (delineated in blue) in contact to a grain of iron (delineated in green) surrounded by olivine in model no. 9. The contrast of velocities at the contact between grains could lead to frictional heating as well as between iron and olivine on the right hand-side of the figure. The white arrow indicates the relative velocity direction.

4.3. Iron/troilite mixtures

In Moreau et al. (2017) we provided a brief first-order estimate of the diffusion of shock induced heat from hot olivine to colder iron. In the models presented here, the same high post-shock temperature contrast exists along iron and troilite grain boundaries. The average of all eutectic models is about 546 K (sd. = 137 K) with the highest, 778 K, from model no. 14, an oblate troilite inclusion in an oblate iron grain.

In Moreau et al. (2017) we treated iron and troilite as isolated phases, which means that effects of eutectic melting were not taken into account. In unshocked ordinary chondrites, these phases are typically not extensively intermixed. Previous thermal and/or shock metamorphic processes have produced mixtures of iron and troilite in about 50% of ordinary chondrites (Schmitt, 1995, 2000; Fujita et al., 1999; Kong and Xie, 2003; Rubin, 2004; Tomkins, 2009; Mare et al., 2014), which then may have been affected by subsequent shock events (Hirata et al., 1995). In our models, by adapting the melting temperature and heat of fusion in mixtures of iron and troilite, melting at lower shock pressures of the two phases may be expected. However, our results show that this is not entirely true for iron. This is because the increase in entropy by the shock wave in iron is too low to reach the eutectic melting temperature and, thus, additional mechanisms are required – such as convergence of shock waves, heat diffusion, frictional heating – or higher shock pressures. This explains why iron sulfides are more abundant in shock-darkening veins in ordinary chondrites than metals,

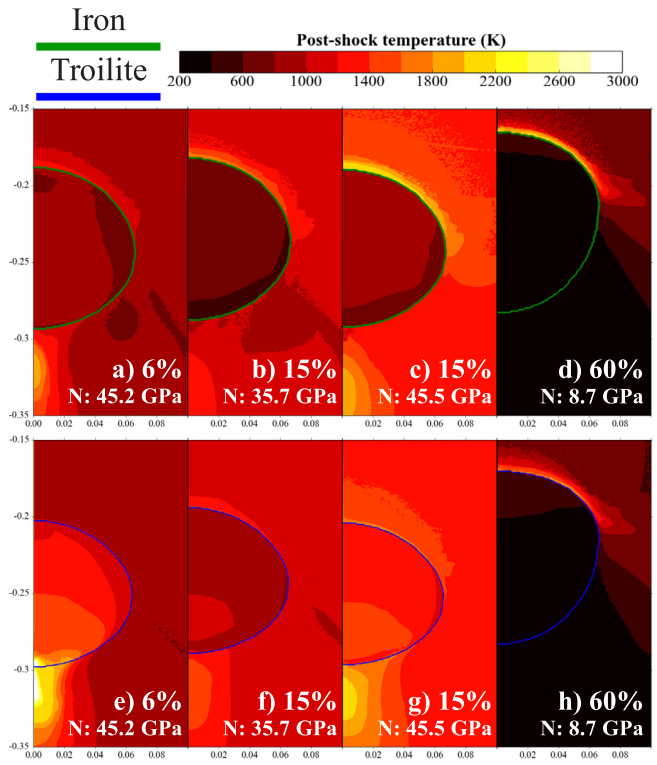

Fig. 9. Post-shock temperature panels for a-d) model no. 1 at 6% porosity olivine, 15% porosity olivine, 15% porosity olivine equalized to 45 GPa nominal pressure (higher flyer plate velocity), and 60% porosity olivine, e-h) model no. 2 at 6% porosity olivine, 15% porosity olivine, 15% porosity olivine equalized to 45 GPa of nominal pressure (higher flyer plate velocity), and 60% porosity olivine. Nominal pressures from a) to b), to d), or e) to f), to h), are different because the flyer plate, at same velocity, generates lower shock pressures in more porous olivine layers. Contour of iron and troilite are given in the figure. The % value is olivine porosity and N is the nominal pressure.

despite metals being more abundant in H and L ordinary chondrites (Stöffler et al. 1991; Xie and Chen, 2016; McSween et al., 1991).

4.4. Effect of porosity and pore crushing

Ordinary chondrites generally exhibit a wide range of porosities (0% to > 20%), depending on the petrographic type, the shock stage and the ordinary chondrite type (Consolmagno et al., 1998, Britt et al., 2002, Britt and Consolmagno, 2003, Sasso et al., 2009). In our work, we assume a rather low porosity of 6% (average measured porosity in H-L chondrites, Britt and Consolmagno, 2003). To conclude our results, we tested a porosity of 15%, and 60% (with cohesive and limited strengths reduced) in olivine within models no. 1 and no. 2 (Fig. 9, see results in Table A4, supplementary material). For the same flyer plate velocity, which generated 45.2 GPa of nominal pressure in all models with 6% porosity in the olivine matrix, we attained a nominal pressure of 35.7 GPa in 15% porous olivine and 8.7 GPa in 60% porous olivine, respectively. As seen in Fig. 9, by pressure reflections, olivine acts mostly as a heat sink at lower porosity with troilite, but may act as a heat source at higher porosity (and lower pressure) for both troilite and iron. This effect increases if we apply higher shock conditions (Fig. 9c and g panels) or higher porosity in olivine (Fig. 9b, d, f and h panels). Increasing the porosity in olivine, thus lowering the nominal pressures, increases also the temperature contrasts between olivine and iron, or troilite, when pressure reflections occur. The propagation of the shock wave, which amounts to the post-heating of olivine, in Fig. 9d and h panels, depends on the impedance contrast existing between the very porous olivine and iron/troilite, which explains the very low temperatures recorded beneath iron/troilite.

We also analysed the effects of pore crushing on an iron layer. The individual pores on top or below iron in models no. 19 and no. 20 would have a volume of 0.00017 mm^3 (cylindrical symmetry applied) which is amongst the most frequent pore volumes found in un-compacted ordinary chondrites (Friedrich et al., 2008) or other petrographic type ordinary chondrites (pore size and geometry, Jones, 2009). Effects of pore crushing were studied in experiments (Kowitz et al., 2013) and mesoscale modelling in sandstones (Güldemeister et al., 2013) and the results of these studies are similar to what we observe in our models. Impact shock is known to produce localized melting (hotspots) at low pressures by pore crushing. Fig. 10 shows the effects of pore crushing within a series of snapshots from model no. 19, in which a pore lies on top of an iron layer. We emphasize here the resulting strong heating/melting of olivine and the localized weak heating/melting of iron. In this case, the hotspot in olivine could easily lead to heat diffusion into iron, causing melting.

4.5. Albite

We have seen that olivine can act as a heat source or sink depending on the shock conditions. This effect of heat source or sink is even more pronounced with albite. Using albite, in models no. 1 and no. 5, brings

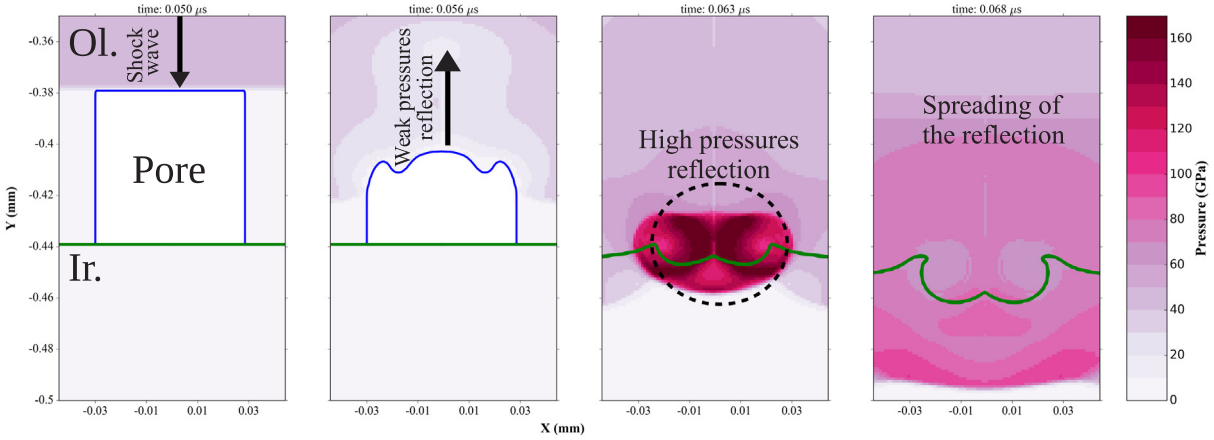

Fig. 10. Snapshots (model no. 19) of a shock wave traveling in the olivine (Ol.) sample reaching an empty pore (delineated in blue) on top of an iron (Ir.) layer. It shows the two stages of pore crushing: low impedance reflection with low pressures followed by a pressure reflection several orders of magnitude higher than the nominal pressure when the pore is closed. The reflected shock wave spreads and then weakens. The snapshots are manually mirrored from the original model at x: 0.00 to have a better view of the effects. The cylindrical symmetry does not provide very accurate pressures along the axis of symmetry, which produces an artefact.

some understanding on currently observed inter-mixed melting of albite and metal or iron (Tomkins, 2009, Tomkins et al., 2013). Two effects that were discussed above must be taken into consideration: the pressure impedance between the different phases and the shock entropy of albite.

1. The impedance contrast between albite and iron, or troilite, and the differences between models no. 1 and 23–24, and models no. 5 and 25–26, show that albite influences the peak shock pressures (heating) and the pressures distribution within troilite and iron. Without exploring the effect further, we observe an increase or decrease of pressures depending on the position of albite to the direction of the shock wave. Also, the contrast of pressure and temperature change highlighted in Fig. 3 in models no. 21 and no. 22, between olivine and albite, illustrates well the importance of pressure effects in spherical grains compared to planar layers.
2. Shock entropy in albite is important to explain the inter-mixed melting of iron, troilite and albite observed in ordinary chondrites. Shock-heating of albite is more important than in olivine, iron, and troilite. In our work, melting of pure albite occurs at ~40 GPa, < ~16 GPa than troilite, which has a melting temperature close to albite. Looking at models no. 2 and no. 22, a grain of albite experiences post-shock temperatures > 100 K than a grain of troilite under the same shock conditions (45.2 GPa nominal pressure and 6% porous olivine). In models 23–26, the temperatures in albite reach very high values and cross the melting temperature of non-eutectic iron and, thus, eventually entraining iron melting by heat diffusion, which explains the observations in Tomkins (2009) and Tomkins et al. (2013).

4.6. Troilite melting

Our previous study (Moreau et al., 2017) claimed that in LL chondrites 20–30% of the whole troilite phase reaches melting temperature at 45 GPa of nominal pressure (rounded troilite grains mostly melted on their own with weak influence of iron). This estimate, however, did not take into account the inhibiting effect of heat of fusion in limiting the extent of melting. Thus with the new procedure we can improve our estimates of the proportion of partial melting. In model no. 2, 27% of troilite material is melting (close to values in Moreau et al., 2017), and yet we provide a partial melt fraction α of 0.14. In this case, only half of the material at melting temperature actually melted after taking into account heat of fusion.

To complete our results, we studied the evolution of troilite melt fraction α over a range of nominal pressures in model no. 2. The resulting melt fractions α are compiled in Fig. 11. We observe that troilite starts to melt at pressures below 35 GPa, up to ~60 GPa, at which point all the material reaches the melting temperature (grey line in Fig. 11) with a melt fraction α equal to 0.77. As we used a Tillotson EoS for this phase, integrating varying heat capacities from Eq. (1) and heat of fusion from Eq. (2) is a necessary step when applying a Tillotson EoS within the iSALE code and working out accurate temperatures and melting. In short, the specific shock energy must be sufficient to reach the melting temperature and then to overcome the heat of fusion to have a fully molten material with α = 1 as calculated in Eq. (2). Such results demonstrate the complexity of shock induced melting in heterogeneous materials. Shock pressures may be amplified due to impedance contrast between different material phases and the geometry of grains, but eutectic melting may play some role, and diffusion of heat and additional heat generation by friction are not negligible to explain shock-darkening in ordinary chondrites. We also show that iron needs pressures much higher that 60 GPa to melt in a single shock event. The model no. 1, with a nominal pressure of 65 GPa, shows no melting of iron. Therefore, all shock pressure amplification effects have to be taken into account to reach melting of iron.

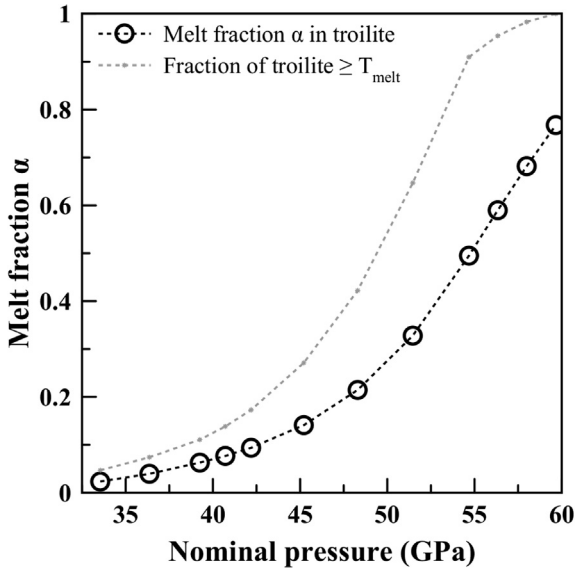

Fig. 11. Profile of troilite melting over nominal pressures in model no. 2. The blank circles are the melt fractions α for the bulk material. The grayed line represents the fraction of material that reaches melting temperature.

4.7. Interpreting shock melting

Comprehending the pressure effects and the precursor material may explain observed melting of iron sulfides and metals in the shock-darkening fabric and the intermixed melt of silicates as presented in this work. However there are observations that we cannot reproduce in our work or that contradict our results, such as melting features described in Fig. 3B in Tomkins (2009), or Fig. 2 in Tomkins et al. (2013) for the NWA 869 meteorite (Metzler et al., 2011). The NWA 869 meteorite is classified as shock stage 3 (15–20 GPa), but containing clasts of higher and undetermined shock stages, such as shock-darkened clasts, from previous impact events on the parent body. The mentioned figures (Tomkins, 2009, Fig. 3B, or Tomkins et al., 2013, Fig. 2) both display metal grains adjacent to troilite grains in a configuration similar to models 7–9. The troilite grains do not show melting features, but the metal grains display an intermixed melt of silicates and metals. The absence of troilite melting might be explained by the shock conditions (15–20 GPa), whereas melting of metals must be explained by other pre-shock or shock mechanisms (e.g. a combination of pore crushing hotspots, plagioclase heating, or very localized concentration of shock waves that ramped up to very high shock pressures). Thus, our results, and observations, can only reproduce simplified conditions of metal, iron sulfide, and silicate melting, and our observations rely on the observations of shock-darkening and the more abundant melting of iron sulfides over metals (Stöffler et al., 1991; Schmitt, 1995, 2000; Xie et al., 2014).

5. Conclusion

We provide more realistic shock-melting simulations through implementing more sophisticated and realistic assumptions on the thermal properties of the mineral phases and by introducing eutectic mixtures of metals and iron sulfides in specific grain configurations. These improvements result in a revised assessment of shock-induced melting of iron sulfides (troilite) and metals (iron) in shock-darkened ordinary chondrites. In all models, troilite is always partially molten at a nominal pressure of 45 GPa. Higher melt fractions are observed, between 0.16 and 0.97, in troilite when it is in eutectic mixtures with iron and mostly embedded in it. In non-eutectic models (isolated troilite grain, or nearby an iron grain), troilite melting occurs with melt fraction between 0.14 and 0.43 maximum. For a nominal pressure of 60 GPa in an

isolated troilite grain we find that the melt fraction reaches a value of 0.77. Iron starts to melt in only a few models at 45 GPa nominal pressure; these models either involve a strong amplification of the shock wave (e.g. in the eutectic mixture of a prolate grain of iron with a troilite inclusion, showing large impedance contrast between the two phases), leading to an increase in shock pressure in iron, or a localized heating by pore crushing. Our results confirm that iron sulfides are the dominant melt fraction over metals in shock-darkened ordinary chondrites with eutectic properties resulting in the melting of metals. We also observed configurations, such as frictional heating or strong diffusion of heat, in which localized melting of metals may occur. Finally, we observed that, at any porosities (6%, 15%, 60%), olivine can act as a heat source for iron and troilite grains due to effects of pressure reflections or concentrations. We also observed that albite is an efficient heat source for iron or troilite, compared to olivine, and can cause melting of any surrounding phases if heated strongly enough.

Acknowledgements

All our thanks go to reviewers, Andy Tomkins and Tom Davison, and Editor Kei Hirose, in contributing to improve our original manuscript. We gratefully acknowledge the developers of iSALE-2D, including Gareth Collins, Kai Wünnemann, Dirk Elbeshausen, Boris Ivanov and Jay Melosh. Some plots in this work were created with the pySALEPlot tool written by Tom Davison. The iSALE-Dellen version was used in this work (Collins et al. 2016).

Fundings

The work was supported by Academy of Finland Project No. 285432. Institute of Geology, the Czech Academy of Sciences is supported by Ministry of Education, Youth and Sports project no. RVO67985831.

Appendix A. Supplementary data

Supplementary data associated with this article can be found, in the online version, at http://dx.doi.org/10.1016/j.pepi.2018.06.006.

References

Ahrens, T.J., Holland, K.G., Chen, G.Q., 1998. Shock temperatures and the melting point of iron. In: Schmidt, S.C., Dandekar, D.P., Forbes,, J.W. (Eds.), Shock Compression of Condensed Matter. AIP Press, Woodbury, NY, pp. 133–136.

Ahrens, T.J., Gregson Jr., V.G., 1964. Shock compression of crustal rocks: data for quartz, calcite, and plagioclase rocks. J. Geophys. Res. 69 (22), 4839–4874.

Amsden A.A., Ruppel H.M., Hirt C.W., 1980. SALE: A simplified ALE computer program for fluid flow at all speeds. Los Alamos, New Mexico: Los Alamos National Laboratory Report LA-8095. p. 101.

Artemieva, N., Ivanov, B., 2004. Launch of Martian meteorites in oblique impacts. Icarus 171, 84–101.

Benusa, M.D., Angel, R.J., Ross, N.L., 2005. Compression of albite, $NaAlSi_3O_8$. Am. Mineral. 90, 1115–1120.

Bland, P.A., Collins, G.S., Davison, T.M., Abreu, N.M., Ciesla, F.J., Muxworthy, A.R., Moore, J., 2014. Pressure–temperature evolution of primordial solar system solids during impact-induced compaction. Nat. Commun. 5, 5451. http://dx.doi.org/10.1038/ncomms6451.

Borg J.P., Chhabildas L.C., 2011. Three-dimensional dynamic loading simulations of sand. In: Schäfer F., Hiermaier S., (Eds.), Proceedings of 11th Hypervelocity Impact Symposium. Schriftenreihe Forschungsergebnisse aus der Kurzzeitdynamik, vol. 20. Freiburg, Fraunhofer EMI. pp. 111–123.

Brace, W.F., Kohlstedt, D.L., 1980. Limits on lithospheric stress imposed by laboratory experiments. J. Geophys. Res. 85 (B11), 6248–6252.

Britt, D.T., Consolmagno, S.J., 2003. Stony meteorite porosities and densities: a review of the data through 2001. Meteorit. Planet. Sci. 38 (8), 1161–1180.

Britt, D.T., Pieters, C.M., Petaev, M.I., Zaslavskaya, N.I., 1989. The Tsarev meteorite – petrology and bidirectional reflectance spectra of a shock-blackened L chondrite. Proc. Lunar Planet. Sci. XIX 537–545.

Britt, D.T., Pieters, C.M., 1989. Bidirectional reflectance characteristics of black chondrite meteorites (abstract). Proc. Lunar Planet. Sci. XX 109–110.

Britt, D.T., Pieters, C.M., 1994. Darkening in black and gas-rich ordinary chondrites: The spectral effects of opaque morphology and distribution. Geochim. Cosmochim. Acta 58 (18), 3905–3919.

Britt, D.T., Yeomans, D., Housen, K., Consolmagno, G., 2002. Asteroid density, porosity, and structure. In: Bottke, W., Cellino, A., Paolicchi, P., Binzel, R.P. (Eds.), Asteroid III. University of Arizona Press, Tuscon, pp. 485–500.

Brown, J.M., Ahrens, T.J., Shampine, D.L., 1984. Hugoniot data for pyrrhotite and the Earth's core. J. Geophys. Res. 89 (B7), 6041–6048.

Chase Jr, M.W., 1998. NIST-JANAF thermochemical tables. monograph 9 In: J. Phys. Chem. Ref. Data, fourth ed. pp. 1–1951.

Chen, J., Rempel, A.W., 2014. Progressive flash heating and the evolution of high-velocity rock friction. J. Geophys. Res. 119 (3182), 3200. http://dx.doi.org/10.1002/2013JB010631.

Christensen, N.I., 1996. Poisson's ratio and crustal seismology. J. Geophys. Res. 101 (B2), 3139–3156.

Collins G.S., Elbeshausen D., Wünnemann K., Davison T.M., Ivanov B., Melosh H.J., 2016. iSALE-Dellen manual: A multi-material, multi-rheology shock physics code for simulating impact phenomena in two and three dimensions. doi:10.6084/m9.figshare.3473690.

Collins, G.S., Melosh, H.J., Ivanov, B.A., 2004. Modeling damage and deformation in impact simulations. Meteorit. Planet. Sci. 39, 217–231.

Collins, G.S., Melosh, H.J., Wünnemann, K., 2011. Improvements to the ε-α porous compaction model for simulating impacts into high-porosity solar system objects. Int. J. Impact Eng. 38 (6), 434–439.

Collins, G.S., Wünnemann, K., Artemieva, N., Pierazzo, E., 2013. Numerical modelling of Impact Processes. In: Osinski, G.R., Pierazzo, E. (Eds.), Impact cratering: Processes and Products, first ed. Blackwell Publishing Lt., pp. 254–270.

Consolmagno, G.J., Britt, D.T., Stoll, C.P., 1998. The porosities of ordinary chondrites: models and interpretation. Meteorit. Planet. Sci. 33, 1221–1229.

Consolmagno, G.J., Britt, D.T., Macke, R.J., 2009. The significance of meteorite density and porosity. Chem. Erde 68, 1–29.

Crawford D.A., Barnouin-Jha O.S., Cintala M.J., 2003. Mesoscale computational investigation of shocked heterogeneous materials with application to large impact craters (abstract #4119). In: 3rd Int. Conf. Large Meteorite Impacts, Nördlingen, Germany. CD-ROM.

Davison, L., 2008. Plane longitudinal shock. In: Fundamentals of Shock Wave Propagation in Solids. Springer-Verlag, Berlin Heidelberg, pp. 37–62.

Davison, T.M., Collins, G.S., Bland, P.A., 2016. Mesoscale modeling of impact compaction of primitive solar system solids. Astrophys. J. 821 (68), 17 10.3847/0004-637X/821/1/68.

Desai, P.D., 1986. Thermodynamic properties of iron and silicon. J. Phys. Chem. Ref. Data 15 (3), 967–983.

Friedrich, J.M., Macke, R.J., Wignarajah, D.P., Rivers, M.L., Britt, D.T., Ebel, D.S., 2008. Pore size distribution in an uncompacted equilibrated ordinary chondrite. Planet. Space Sci. 56, 895–900.

Fritz, J., Artemieva, N., Greshake, A., 2005. Ejection of Martian meteorites. Meteorit. Planet. Sci. 40 (9/10), 1393–1411.

Fujita, T., Kojima, H., Yanai, K., 1999. Origin of metal-troilite aggregates in six ordinary chondrites. Antarct. Meteorite Res. 12, 19–35.

Gillet, P., Richet, P., Guyot, F., Fiquet, G., 1991. High-temperature thermodynamic properties of forsterite. J. Geophys. Res. 96 (B7), 11805–11816.

Güldemeister, N., Wünnemann, K., Durr, N., Hiermaier, S., 2013. Propagation of impact-induced shock waves in porous sandstone using mesoscale modeling. Meteorit. Planet. Sci. 48 (1), 115–133.

Hemingway, B.S., Krupka, K.M., Robie, R.A., 1981. Heat capacities of the alkali feldspars between 350 and 1000 K from differential scanning calorimetry, the thermodynamic functions of the alkali feldspars from 298.15 to 1400 K, and the reaction quartz + jadeite = analbite. Am. Mineral. 66, 1202–1215.

Heymann, D., 1967. On the origin of hypersthene chondrites: ages and shock effects of black chondrites. Icarus 6, 189–221.

Hirata, N., Kurita, K., Sekine, T., 1995. Shock experiments on silicate-metal-sulfide powder mixture: Effect of low eutectic temperature of sulfide-metal system. Proc. Lunar Planet. Sci. XXVIII 44–47.

Hirose, A., Lonngren, K., 1985. Introduction to Wave Phenomena. J. Willey & Sons, New York.

Ivanov, B.A., 2005. Shock melting of permafrost on Mars: water ice multiphase equation of state for numerical modeling and its testing. Lunar Planet. Sci. XXXVIII. Lunar Planet. Inst., Houston #1232(abstr.), CD-ROM.

Ivanov, B.A., Deniem, D., Neukum, G., 1997. Implementation of dynamic strength models into 2D hydrocodes: applications for atmospheric breakup and impact cratering. Int. J. Impact Eng. 20, 411–430.

Jones, S.F., 2009. Elastic Wave Velocity, Porosity, and Pore Geometry of Ordinary Chondrites and Artificially Shocked Samples. University of Calgary, Department of Geosciences, pp. 178 Thesis.

Keil, K., Jeffrey, F.B., Britt, D.T., 1992. Reflection spectra of shocked ordinary chondrites and their relationship to asteroids. Icarus 98, 43–53.

Kohout, T., Gritsevich, M., Grokhovsky, V.I., Yakokiev, G.A., Haloda, J., Halodova, P., Michallik, R.M., Penttilä, A., Muinonen, K., 2014. Mineralogy, reflectance spectra, and physical properties of the Chelyabinsk LL5 chondrite – Insight into shock-induced changes in asteroid regoliths. Icarus 228, 78–85. http://dx.doi.org/10.1016/j.icarus.2013.09.027.

Kojitani, H., Akaogi, M., 1995. Measurement of heat of fusion of model basalt in the system diposide – forsterite – anorthite. Geophys. Res. Lett. 22 (17), 2329–2332.

Kong, P., Xie, X., 2003. Redistribution of elements in the heavily shocked Yanzhuang chondrite. Meteorit. Planet. Sci. 38 (5), 739–746.

Kowitz, A., Schmitt, R.T., Reimold, W.U., Hornemann, U., 2013. The first MEMIN shock recovery experiments at low shock pressure (5–12.5 GPa) with dry, porous sandstone. Meteorit. Planet. Sci. 48 (1), 99–114.

Kozlov, E.A., Petrovtsev, A.V., 2014. Cumulation of a spherically converging shock wave

in metals and its dependence on elastic-plastic properties, phase transitions, spall and shear fractures. J. Phys. Conf. Ser. 490. http://dx.doi.org/10.1088/1742-6596/490/1/012191.
Langenhorst, F., Deutsch, A., 1994. Shock experiments on pre-heated alpha- and beta-quartz; I, optical and density data. Earth Planet. Sci. Lett. 125, 407–420.
Langenhorst, F., Hornemann, U., 2005. Shock experiments on minerals: basic physics and techniques. EMU Notes Mineral. 7 (15), 357–387.
Lehner, S.W., Buseck, P.R., McDonough, W.F., 2010. Origin of kamacite, schreibersite, and perryite in metal-sulfide nodules of the enstatit chondrite Sahara 97072 (EH3). Meteorit. Planet. Sci. 45 (2), 289–303.
Louzada, K.L., Stewart, S.T., Weiss, B.P., Gattacceca, J., Bezaeva, N.S., 2010. Shock and static pressure demagnetization of pyrrhotite and implications for the Martian crust. Earth Planet. Sci. Lett. 290, 90–101.
Mare, E.R., Tomkins, A.G., Godel, B.M., 2014. Restriction of parent body heating by metal-troilite melting: thermal models for the ordinary chondrites. Meteorit. Planet. Sci. 49 (4), 636–651.
McQueen, R.G., Marsh, S.P., Fritz, J.N., 1967. Hugoniot equation of state of twelve rocks. J. Geophys. Res. 72 (20), 4999–5036.
McSween Jr., H.Y., Bennett III, M.E., Jarosewich, E., 1991. The mineralogy of ordinary chondrites and implications for asteroid spectrophotometry. Icarus 90 (1), 107–116.
Melosh, H.J., 1989. Impact cratering: a geologic process. Oxford Monogr. Geol. Geophys. 11, 253 pp.
Melosh, H.J., 2005. The Mechanics of Pseudotachylite Formation in Impact Events. In: Koeberl, C., Henkel, H. (Eds.), Impact Tectonics. Springer, Berlin Heidelberg, Berlin, Germany, pp. 55–80.
Melosh, H.J., 2007. A hydrocode equation of state for SiO2. Meteorit. Planet. Sci. 42 (12), 2079–2098.
Melosh, H.J., Ryan, E.V., Asphaug, E., 1992. Dynamic fragmentation in impacts: hydrocode simulation of laboratory impacts. J. Geophys. Res. 97 (E9), 14735–14759.
Metzler, K., Bischoff, A., Greenwood, R.C., Palme, H., Gellissen, M., Hopp, J., Franchi, I.A., Trieloff, M., 2011. The L3–6 chondritic regolith breccia Northwest Africa (NWA) 869: (I) Petrology, chemistry, oxygen isotopes, and Ar-Ar age determinations. Meteorit. Planet. Sci. 46 (5), 652–680.
Meyer, C., Fritz, J., Misgaiski, M., Stöffler, D., Artemieva, N.A., Hornemann, U., Moeller, R., Vera, J.-P.-de, Cockell, C., Horneck, G., Ott, S., Rabbow, E., 2011. Shock experiments in support of the Lithopanspermia theory: the influence of host rock composition, temperature, and shock pressure on the survival rate of endolithic and epilithic microorganisms. Meteorit. Planet. Sci. 46 (5), 701–718. http://dx.doi.org/10.1111/j.1945-5100.2011.01184.x.
Moreau, J., Kohout, T., Wünnemann, K., 2017. Shock-darkening in ordinary chondrites: determination of the pressure-temperature conditions by shock physics mesoscale modeling. Meteorit. Planet. Sci. 52 (11), 2375–2390. http://dx.doi.org/10.1111/maps.12935.
Perras, M.A., Diederichs, M.S., 2014. A review of the tensile strength of rock: concepts and testing. Geotech. Geol. Eng. 32, 525–546. http://dx.doi.org/10.1007/s10706-014-9732-0.
Prescher, C., Langenhorst, F., Hornemann, U., Deutsch, A., 2011. Shock experiments on anhydrite and new constraints on the impact-induced SO_x release at the K-Pg boundary. Meteorit. Planet. Sci. 11, 1619–1629.
Rajendran, A.M., Grove, D.J., Dietenberger, M.A., Cook, W.H., 1990. In: A Dynamic Failure Model for Ductile Materials. University of Dayton Research Institute, Air Force Armament Laboratory, Dayton, Ohio, pp. 45469–50120.
Riedel, W., Wicklein, M., Thoma, K., 2008. Shock properties of conventional and high strength concrete, experimental and mesomechanical analysis. Int. J. Impact Eng. 35, 155–171. http://dx.doi.org/10.1016/j.ijimpeng. 2007.02.001.
Rubin, A.E., 2004. Postshock annealing and postannealing shock in equilibrated ordinary chondrites: Implications for the thermal and shock histories of chondritic asteroids. Geochim. Cosmochim. Acta 68, 673–689.
Sasso, M.R., Macke, R.J., Boesenberg, J.S., Britt, D.T., Rivers, M.L., Ebel, D.S., Friedrich, J.M., 2009. Incompletely compacted equilibrated ordinary chondrites. Meteorit. Planet. Sci. 44 (11), 1743–1753.
Schmitt, R.T., 1995. Experimentelle und theoretische Untersuchungen zur Stoßwellenmetamorphose von gewöhnlichen Chondriten. Ph.D. thesis. Westfälischen Wilhelms-Universität, Münster, Germany.
Schmitt, R.T., 2000. Shock experiments with the H6 chondrites Kernouvé: pressure calibration of microscopic shock effects. Meteorit. Planet. Sci. 35, 545–560.
Sharma, R., Chang, Y., 1979. Thermodynamics and phase relationships of transition metal-sulfur systems: Part III. thermodynamic properties of the Fe-S liquid phase and the calculation of the Fe-S phase diagram. Metall. Mater. Trans. B 10, 103–108.
Sharp, W.E., 1969. Melting curves of sphalerite, galena, and pyrrhotite and the decomposition curve of pyrite between 30 and 65 kilobars. J. Geophys. Res. 74 (6), 1645–1652.
Stöffler, D., Keil, K., Edward, S., 1991. Shock metamorphism of ordinary chondrites. Geochim. Cosmochim. Acta 55 (12), 3845–3867.
Tenner, T.J., Lange, R.A., Downs, R.T., 2007. The albite fusion curve re-examined: new experiments and the high pressure density and compressibility of high albite and $NaAlSi_3O_8$ liquid. Am. Mineral. 92, 1573–1585.
Thompson, S.L., 1990. ANEOS Analytic Equations of State for Shock Physics Codes Input Manual. Computational Physics and Mechanics Division I, Sandia National Laboratories, Albuquerque, New Mexico.
Tomkins, A.G., 2009. What metal-troilite textures can tell us about post-impact metamorphism in chondrite meteorites. Meteorit. Planet. Sci. 44 (8), 1133–1149.
Tomkins, A.G., Weinberg, R.F., Schaefer, B.F., Langendam, A., 2013. Disequelebrium melting and melt migration driven by impacts: implications for rapid planetesimal core formation. Geochim. Cosmochim. Acta 100, 41–59.
Trunin, R.F., 2001. In: Experimental Data on Shock Compression and Adiabatic Expansion of Condensed Matter. RFNC-VNIIEF, Sarov, Russia, pp. 446.
van der Bogert, C.H., Schultz, P.H., Spray, J.G., 2003. Impact-induced frictional melting in ordinary chondrites: a mechanism for deformation, darkening, and vein formation. Meteorit. Planet. Sci. 38 (10), 1521–1531.
Wünnemann, K., Collins, G., Melosh, H., 2006. A strain-based porosity model for use in hydrocode simulations of impact and implication for transient crater growth in porous targets. Icarus 180, 514–527.
Xie, X., Chen, M., 2016. In: Suizhou Meteorite: Mineralogy and Shock Metamorphism. Springer-Verlag Berlin and Heidelberg, pp. 258. http://dx.doi.org/10.1007/978-3-662-48479-1.
Xie, X., Chen, M., Zhai, S., Wang, F., 2014. Eutectic metal + troilite + Fe-Mn-Na phosphate + Al-free chromite assemblage in shock-produced chondritic melt of the Yanzhuang chondrite. Meteoriti. Planet. Sci. 49 (12), 2290–2304.